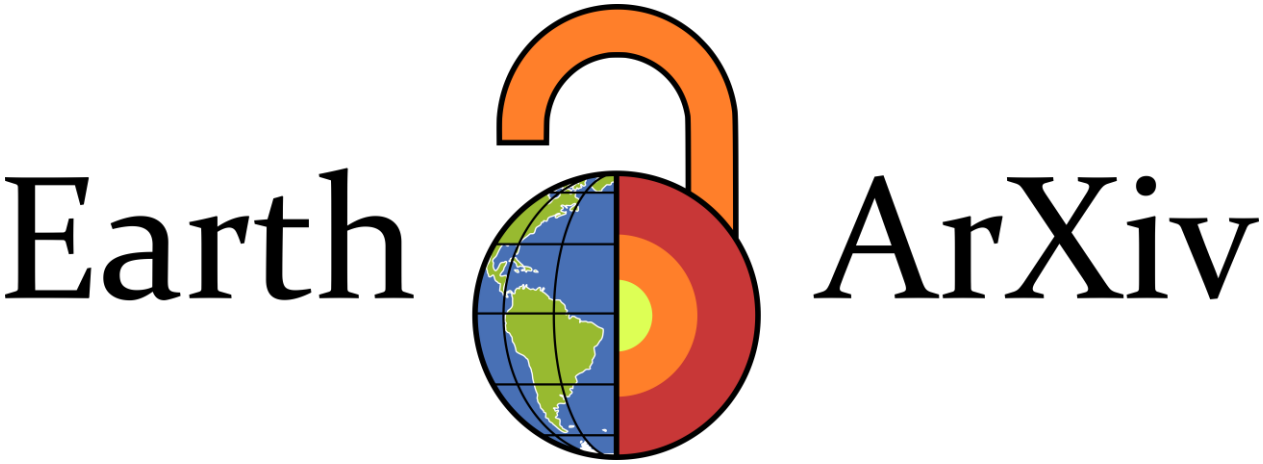

5

---

10 This manuscript will be submitted for publication in Atmospheric Measurement Techniques. Please note the manuscript has yet to be formally accepted for publication. Subsequent versions of this manuscript may have slightly different content. If accepted, the final version of this manuscript will be available via the 'Peer-reviewed Publication DOI' link
15 on the right-hand side of this webpage. Please feel free to contact any of the authors; we welcome feedback.

Performance validation of the GHGSat Methane Constellation via controlled releases

Antoine Ramier[1], Hanford Deglint[1], Ariane Deslieres[1], Lia Formenti[1], Marianne Girard[1], Dylan Jervis[1], David J. Marshall[1], Jean-Philippe W. MacLean[1], Jason McKeever[1], Andrew McKell[1], Mathias Strupler[1], Ewan Tarrant[1]

[1]GHGSat Inc. Montreal, QC, Canada, H2W 1Y5

Correspondence to: Antoine Ramier (aramier@ghgsat.com)

Abstract. Satellite remote sensing has become an important tool for detecting, quantifying, and attributing methane emissions, yet a rigorous, condition-dependent characterization of point-source imager performance has not previously been established, despite being essential to support its use in regulatory and voluntary reporting frameworks. We present a comprehensive performance assessment of the GHGSat constellation of high-resolution methane-imaging satellites based on a multi-campaign controlled release dataset spanning 2021 to 2026 that combines self-organized campaigns with independent third-party experiments. We develop a probabilistic, environmental conditions-dependent detection model in which the probability of detection depends on the plume signal to noise ratio (SNR), which is in turn a function of emission rate, wind speed, retrieval noise, and spatial resolution. We find that an SNR of 1.72 ± 0.39 is required to achieve a 50% probability of detection, which translates to a detection limit $Q_{50} = 99.0 \pm 5.3$ kg h^{-1} in median environmental conditions encountered in controlled releases (3 m s^{-1} wind speed, 7 mmol m^{-2} column density noise, 27 m resolution). The estimated Q_{50} is shown to converge stably as data accumulate and to remain consistent when blind validation samples are added to self-organized releases. Quantification accuracy is evaluated through parity analysis of estimated versus metered emission rates, yielding an ordinary least squares slope of 0.93 ± 0.03 and R^2 of 0.92 using reported model winds, improving to 0.96 ± 0.02 and $R^2 = 0.95$ with a co-located anemometer. A comparison of emission rate estimates based on ERA5, IFS, and HRRR winds shows that quantification accuracy is largely insensitive to the choice of operationally available wind product, with a residual underestimation at low emission rates that correlates with wind model spatial resolution. We further demonstrate a bias correction combining a local concentration background correction with an empirically recalibrated effective wind speed, which recovers the low-rate sources that were previously underestimated and removes most of the residual bias without degrading accuracy at higher emission rates. These results establish a transparent, statistically grounded baseline for the GHGSat constellation's detection and quantification performance and provide a methodological framework that can be extended as additional controlled-release data become available.

1 Introduction

Methane (CH_4) is the second most important anthropogenic contributor to global warming after carbon dioxide, responsible for approximately 20–30 % of the total anthropogenic increase in radiative forcing since pre-industrial times (Intergovernmental Panel on Climate Change (IPCC), 2023; Saunois et al., 2025). Its relatively short mean atmospheric lifespan (~10 years) and strong global warming potential (80 times that of CO_2 over a 20-year period) make near-term reductions in methane emissions a critical lever for limiting the pace of climate change. A growing body of sector-specific regulations and voluntary frameworks reinforces this commitment, with industrial actors across the energy and waste sectors increasingly required – or choosing – to monitor, report, and mitigate their methane footprints.

Satellite-borne remote sensing has become an important tool for methane monitoring, providing spatially extensive observations that complement ground-based, airborne, and facility-level measurement approaches. By detecting, quantifying, and localizing emissions over large areas and repeated observation campaigns, satellite observations can support emissions reporting and inventory development, advance scientific understanding of emission processes and magnitudes, and can inform targeted mitigation actions by pinpointing large, previously unidentified sources (Jacob et al., 2016). GHGSat was among the first organizations to demonstrate high-resolution methane sensing from space. Its first demonstration satellite, GHGSat-D "Claire", was launched in June 2016, establishing the feasibility of facility-scale methane detection and quantification from orbit (Jervis et al., 2021). Since then, GHGSat has built and deployed a commercial constellation which currently comprises 15 satellites in low Earth orbit.

Methane point-source imagers – including GHGSat, other purpose-built instruments such as Tanager, and public satellites not originally intended for methane measurement such as EMIT, EnMAP, PRISMA, Sentinel-2, and Landsat-8 – are validated and compared on two end-user metrics: the probability of detection (PoD), which characterizes the ability of a system to detect emissions in a noisy background; and the quantification accuracy, which characterizes how faithfully the estimated emission rate reflects the true source rate. Both metrics are assessed through controlled releases, in which a precisely metered flow of methane is emitted at a known location and time while the sensor system attempts to detect and quantify the release. Because the source rate and observing geometry are independently known, controlled releases provide one of the most direct means of evaluating methane-imaging performance (Bell et al., 2022; Brandt et al., 2026; Chen et al., 2024; Conrad et al., 2023; El Abbadi et al., 2024; Sherwin et al., 2021, 2023, 2024; Thorpe et al., 2016, 2024).

This article presents an analysis of the GHGSat constellation performance based on a multi-campaign controlled release dataset spanning 2021 to 2026, combining both self-organized and third-party campaigns. We introduce a probabilistic, environmental conditions-dependent model based on the mass-balance heuristic from Jacob et al. (2016) to describe the detection performance of the GHGSat constellation. Comparing multiple variants of this model based on the Akaike and Bayesian information criteria, we find the PoD to be well-described by a log-normal function of the ratio of source rate (q) over retrieval noise (n), spatial resolution, and wind speed (u) with a linear offset parameter (u_0). The best-fit model through maximum likelihood implies a 50% probability of detecting an emission rate of 99.0 ± 5.3 kg h^{-1} in a wind speed of 3 m s^{-1}

and a median CH_4 column error of 7.0 mmol m^{-2}. We demonstrate that this estimate converges stably over time and remains highly consistent as independent blind validation is added to the self-organized releases. We also evaluate quantification accuracy through a parity analysis comparing GHGSat-estimated emission rates across all campaigns.

2 Controlled release methods and dataset

The results and analyses presented in this article draw on a compilation of controlled-release campaigns, summarized in Table 1. Measurement data from all satellites that use the current version of the GHGSat methane-sensing spectrometer (GHGSat-C2 and above) are included.

Table 1. Summary of controlled release campaigns for the GHGSat constellation

Dates	Organizer	Location	Blindness	TP	FN	TN	FP	Tot.	References
2021-03–2025-07	GHGSat/CMC	Brooks, AB	Pseudo	28	17	0	0	45	*This article*
2021-10–2021-11	Stanford	Ehrenberg, AZ	Single	3	0	0	0	3	(Sherwin et al., 2023)
2022-10–2022-11	Stanford	Casa Grande, AZ	Single	1	0	1	0	2	(Sherwin et al., 2024)
2024-08–2024-10	Stanford	Evanston, WY	Pseudo	6	5	2	0	13	(Brandt et al., 2026)
2024-11–2024-12	Stanford	Casa Grande, AZ	Pseudo	5	2	0	0	7	(Brandt et al., 2026)
2025-01–2025-12	Stanford	Casa Grande, AZ	Single	47	4	8	1	60	(Brandt et al., 2026)
2025-05–2025-06	FluxLab	Petrolia, ON	Single	3	2	0	0	5	(FluxLab and Tarek, 2026)
2025-06–2025-06	TADI/Stanford	Lacq, France	Single	1	1	3	0	5	*To be published*
Total				94	31	14	1	140	

We distinguish two types of experiments: single-blind and pseudo-blind. In a single-blind experiment, an independent third party organizes the campaign and performs ground operations and reference measurements; the measurement provider (GHGSat) is kept unaware of the emission rate, its precise location, and the presence or absence of a release. GHGSat has participated in several such blind studies, including the campaigns organized by Stanford University (Sherwin et al., 2023, 2024; Brandt et al., 2026), FluxLab (Bourlon et al., 2026; FluxLab and Tarek, 2026), and the TotalEnergies Anomalies Detection Initiatives (McManemin et al., 2026). Before the large-scale ramp-up of blind samples in 2024–2025, the need for self-validation motivated a series of campaigns between 2021 and 2025, organized in partnership with Carbon Management Canada (CMC) and the University of Calgary at the Atmospheric Fugitive Emission (AFE) test facility near Brooks, Alberta. These campaigns are not strictly blind – GHGSat co-organized them and participated in ground operations – but for performance analysis the measurements were processed in a pseudo-blind manner, using the same inspection and quantification methods as in a blind experiment or routine operations. We also label as pseudo-blind the "phase 0" of the Stanford study at

the Wyoming and Arizona sites, since results from this preparatory phase were openly shared between the organizers and participating teams.

2.1 Controlled releases at the Carbon Management Canada facility

Controlled release measurements were conducted at Carbon Management Canada's field research station, located near Brooks, Alberta, Canada, shown in Fig. 1 (Anon, 2025; Blackmore et al., 2025; Wigle et al., 2024). The surrounding landscape is mostly flat open grassland. Compressed natural gas (CNG) was transported to the controlled release site using a trailer that was outfitted with 16 high pressure cylinders. Each canister has a seamless aluminum liner and is entirely overwrapped with high-strength carbon fiber embedded in an epoxy resin matrix allowing for a pressure rating of 3,600 PSIG. After each trailer refill the CNG composition was analyzed at the Isotope Science Lab and the University of Calgary. The released gas consisted of an average of ~94% CH_4 by volume, with remaining constitutes being ethane (~3.5% by volume), propane (~1% by volume), and other minor components (~1.5% by volume) such as heavier hydrocarbons, N_2, and O_2.

The gas was released from the pressurized cylinder via a regulator valve. The temperature of the expanding gas decreases due to the Joule-Thomson effect; the gas temperature was conditioned to atmospheric temperature by means of a heat exchanger. The release rate was controlled by adjusting the pressure regulator and measured using the FloBoss™ 103 (a calibrated flow computer) coupled with a McCrometer v-cone flow meter (½" and 1", depending on the desired flow rate). The flow rate was visually inspected and logged digitally during the releases. Finally, the conditioned CNG was vented to atmosphere via a modular stack at two heights: 3.4 m and 4.8 m. All components were connected using high pressure red polyurethane jacketed flowlines constructed of electrically conductive nylon core and steel braided reinforcement layer. The local meteorological conditions were measured using portable 81000-L RM Young 3D ultrasonic anemometer, situated 2.25 m above ground.

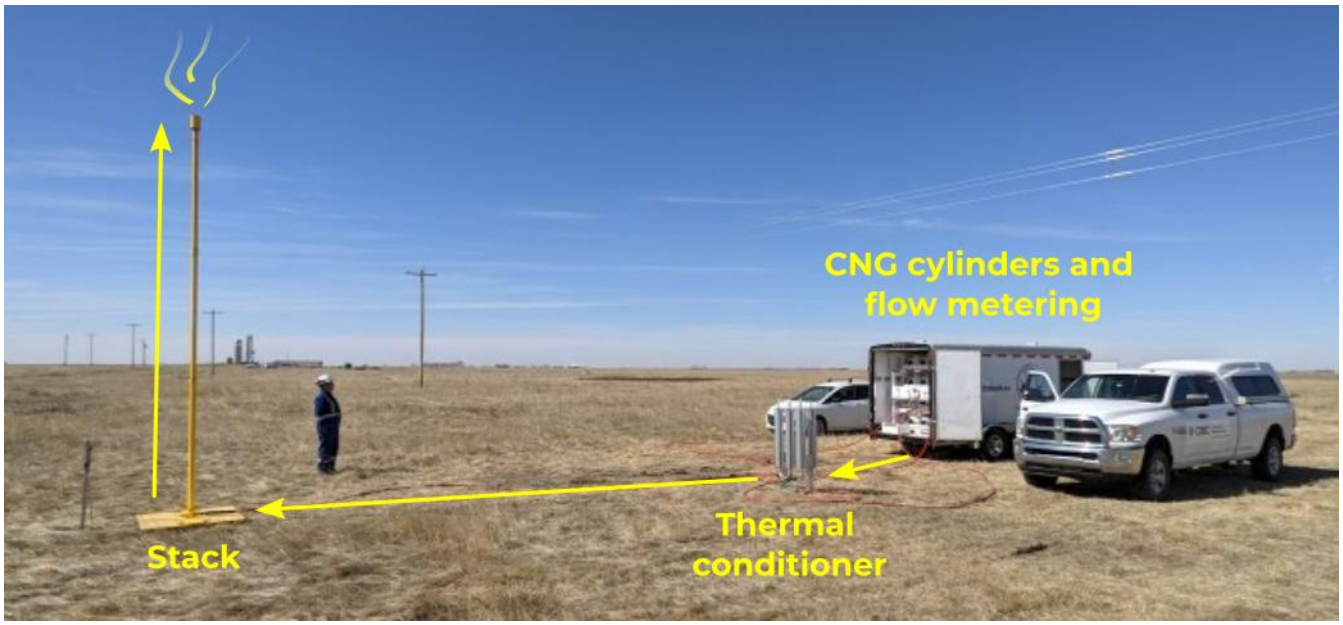

Figure 1: Overview of the controlled release set-up. Visible are the yellow-painted modular stack (left), the conditioner (center), and the trailer housing the cylinders with CNG, pressure regulators, and flow meters (right). All components are connected using high-pressure gas lines (in red).

2.2 Satellite data acquisition

GHGSat satellites measure the methane concentration in the atmosphere based on the general principle of absorption spectroscopy. The main optical payload is a wide-angle Fabry-Pérot (WAF-P) interferometer, which provides spectrally resolved measurements of backscattered sunlight in the shortwave infrared (SWIR), targeting methane-specific absorption lines around 1.6 µm (Jervis et al., 2021).

GHGSat satellites operate in target mode, collecting multiple partially overlapping camera frames over a 20 s acquisition window. During that time, the field of view is translated along the direction of satellite motion at a rate much slower than the orbital velocity, allowing optical signal to be collected over each ground point for a longer interval than nadir-pointing would permit. Target-pointing maneuvers and acquisition settings during controlled releases matched those of standard commercial operations.

Unlike global imagers, which survey the whole Earth periodically, GHGSat observations are tasked in advance for specific targets. Controlled-release opportunities were therefore coordinated between GHGSat mission planning and the partner ground team, balancing upcoming orbital overpasses, weather forecasts, commercial scheduling constraints, and the availability of ground staff at the release facility.

After each observation, the raw level 0 (L0) data are downlinked and processed by GHGSat's proprietary toolchain to produce the deliverable L2 products (spatially resolved albedo, methane enhancement, and uncertainty) and L4 products (emission identification and quantification).

2.3 Source identification and quantification

Emission plumes are identified based on methane enhancement, its associated uncertainty, and the albedo. To distinguish true methane enhancements from noise and artifacts, the spatial structure of the plume (general morphology, alignment with the wind direction) is assessed, and the enhancement should not correlate with features present in the albedo layer. Inspection of the albedo field and publicly available imagery of the surveyed sites provides additional contextual information on the presence or absence of potential methane-emitting sources.

Once an emission plume is identified, the methane emission rate is estimated using the integrated mass enhancement (IME) method (Varon et al., 2018). We define the integral of column density enhancements over the visible extent of the plume:

$$\mathrm{IME} = \int_{M_p} \Omega(x, y)\ dy\ dx, \tag{1}$$

where the integration domain M_p is a plume "mask" in which the enhancements are visible above the noise level. The IME quantifies the local accumulation of methane and is driven by two factors: the actual emission rate q, and the rate at which the methane dissipates in the surrounding atmosphere, which in turn is driven by wind speed u. Those quantities are related mathematically through the equation

$$q = \frac{U_{\mathrm{eff}}(u_{10})}{L_{\mathrm{eff}}}\ \mathrm{IME}, \tag{2}$$

where q is the emission rate, U_{eff} is the effective wind speed, and $L_{\mathrm{eff}} = \sqrt{A}$ is an effective plume length defined as the square root of the area of the plume mask. The effective wind speed is expressed as a function of the wind speed at 10 m above ground u_{10}, a quantity available from most global weather models, through an empirical relationship obtained from a large ensemble of simulations (Maasakkers et al., 2022; Varon et al., 2018):

$$U_{\mathrm{eff}} = 0.34\ u_{10} + 0.42. \tag{3}$$

Plume masks are generated in four steps: Gaussian filtering for noise suppression, thresholding against the local noise level, rejecting pixels that are not connected to the plume origin, and connecting disjoint "puffs" using binary dilation. The method is semi-automated: it provides reasonable default parameters at each step but allows GHGSat analysts to adjust them so that only real enhancements – not albedo-correlated artifacts – are included in the mask. Example plumes over different release locations are provided in Fig. 2 with their associated masks and emission rates.

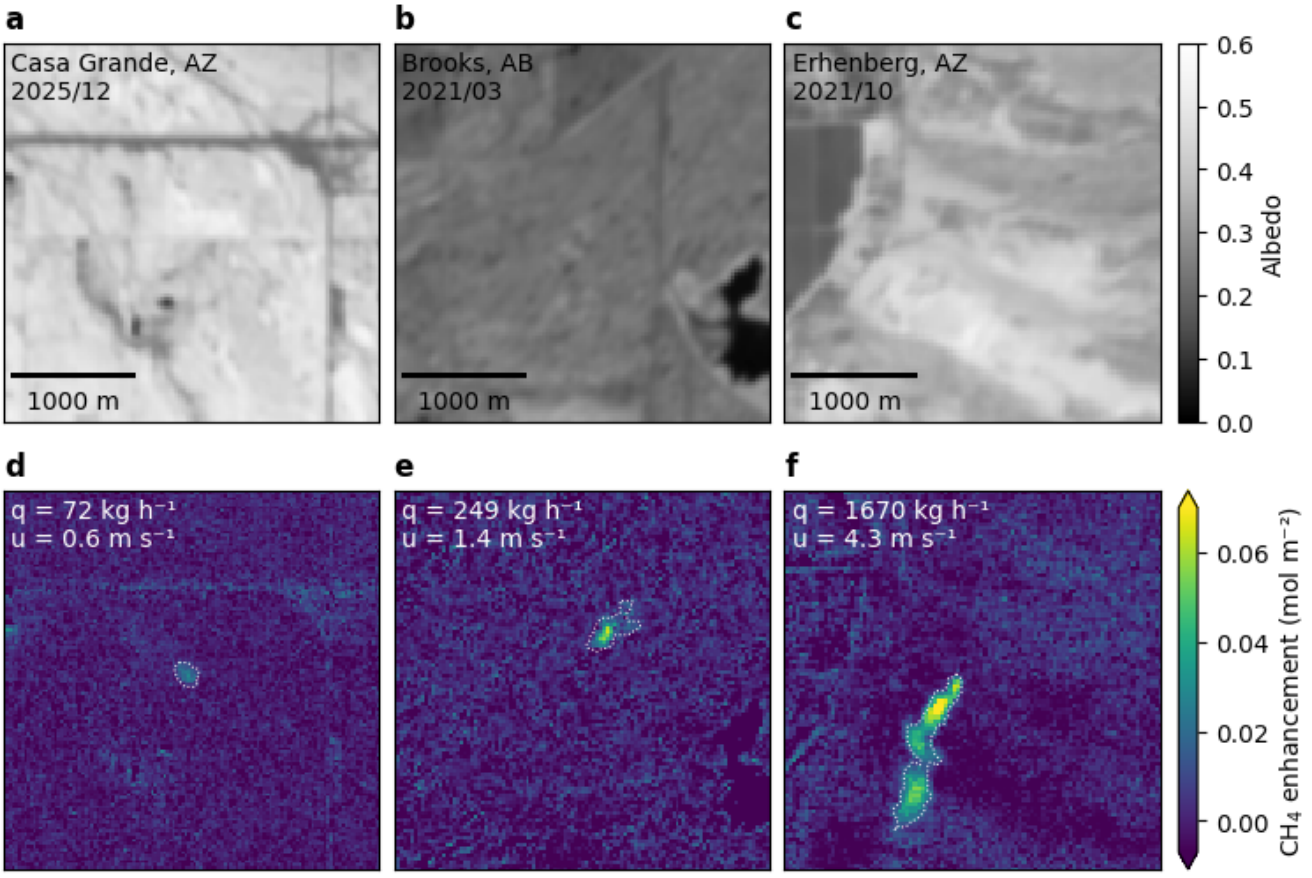

Figure 2. Example emission masks and rate estimates for 3 controlled release events. (a)-(c) Retrieved albedo of the 3 release sites. (d)-(f) Corresponding methane enhancement and plume mask boundaries (dotted white line). The location and date of the release are labelled on the albedo panels, while the emission rate *q* and wind speed *u* are listed on the methane panels.

3 Detection performance

3.1 Conditions-dependent probability of detection

The detection capability of a remote-sensing system is commonly characterized by its probability of detection (PoD). High-level performance metrics such as Q_{50} and Q_{90} – detection limits at a probability of 50% or 90% respectively – can be useful for comparing systems. However, advanced quantitative applications such as building measurement-informed emission inventories require a more rigorous description that incorporates two key features (McKeever and Jervis, 2025). First, the detection limit is conditions-dependent, varying with both environmental and operational factors. Second, detection is probabilistic: small emissions have a lower probability of being detected than large ones, but the transition is smooth rather than a hard cutoff.

Here we use a probabilistic formalism following (Conrad et al., 2023; Manninen et al., 2026; Thorpe et al., 2024), where we express the probability of detection as

$$\mathrm{PoD} = P(Z(\boldsymbol{X};\boldsymbol{\phi});\boldsymbol{\theta}), \tag{4}$$

which is the composition of two functions commonly referred to as the predictor function $Z(\boldsymbol{X};\boldsymbol{\phi})$ and the inverse-link probability function $P(Z;\boldsymbol{\theta})$. Conceptually, $Z(\boldsymbol{X};\boldsymbol{\phi})$ models how a vector $\boldsymbol{X}$ of observation-specific, environmental and operational variables (emission rate, wind speed, etc.) affect how detectable an emission is at processing level 2. On the other hand, the function $P(Z;\boldsymbol{\theta})$ smoothly maps the predictor to a normalized probability. Its parameters $\boldsymbol{\theta}$ characterize the "inspection" process (level 4), and may be affected by the type of processing (automated vs. manual) and the quality of prior information (presence or absence of known potential emitter). The vectors $\boldsymbol{\phi}$ and $\boldsymbol{\theta}$ are model parameters which can be obtained by fitting to binary results of controlled releases, maximizing the likelihood $\mathcal{L}$ – or equivalently minimizing the negative log-likelihood (NLL) – of a sequence of independent Bernoulli trials:

$$\mathrm{NLL} = -\ln\mathcal{L} = -\sum_{i\in\{\mathrm{TP},\mathrm{FN}\}} d_i \ln p_i + (1-d_i)\ln(1-p_i)\,, \tag{5}$$

where the summation is carried over the true positive (TP) and false negative (FN) controlled release results, d_i is the binary detection result, and $p_i = P(Z(\boldsymbol{X}_i;\boldsymbol{\phi});\boldsymbol{\theta})$ is the probability of detection model evaluated at the set of environmental parameters for each specific release $\boldsymbol{X}_i$. The choice of appropriate parameters and functional forms for the predictor and link functions requires consideration and is examined in the following sections.

3.1.1 Predictor variables

Jacob et al. (2016), introduced a useful heuristic for the detection limit by estimating the peak methane enhancement from a point source in a uniform wind field, and imposing a minimum signal to noise ratio for the detection. With minor changes to the original publication in terms of units and variable rearrangement, this heuristic can be expressed in the following form:

$$Z = \frac{q}{u\,n\,a}, \tag{6}$$

where q is the emission rate (mol s^{-1}), u is the wind speed (m s^{-1}), n is the noise on the measured methane column density (mol m^{-2}), a is the spatial resolution of the instrument (m), and Z is an dimensionless quantity representing the signal to noise ratio of the highest plume enhancement, providing a measure of plume "detectability" (Bruno et al., 2024; Manninen et al., 2026).

Importantly, the Jacob heuristic identifies the set of parameters $\boldsymbol{X} = \{q, u, n, a\}$ upon which the PoD should depend, excluding higher order effects. Other parameters commonly identified as drivers of detection performance – surface albedo, topography, solar and viewing angles, scan panning speed, sensor-to-ground distance, meteorological conditions, atmospheric composition, and camera settings – are intermediate variables that act through either the spatial resolution or the noise. This makes it possible to conceptualize a conditions-dependent model that is simple enough to constrain via controlled-release data, yet broadly applicable across operational conditions (Thorpe et al., 2024).

To assess the relative predictive strength of each variable, our analysis evaluates several subsets of the four core parameters: $\boldsymbol{X} = \{q\}$ (a plain regression as a function of source rate); $\boldsymbol{X} = \{q, u\}$ (a commonly assumed dependence on q/u); other possible 2- and 3-variables subsets; and the full set $\boldsymbol{X} = \{q, u, n, a\}$.

In this study, the source rate q is defined as the time average of the flow rate reported by the flowmeter $q_{\mathrm{fm}}(t)$, over an integrating window starting T minutes before the observation and ending at the observation time t_{obs}:

$$q = \frac{1}{T}\int_{t_{\mathrm{obs}}-T}^{t_{\mathrm{obs}}} q_{\mathrm{fm}}(t)\, dt. \tag{7}$$

The wind speed u is obtained by applying the same averaging window to the magnitude of the local wind time series $u_{\mathrm{lw}}(t)$ measured by the anemometer. We used an integrating window length of 5 minutes, ensuring consistency with published datasets (Sherwin et al., 2023, 2024).

The spatial resolution metric a is the 1-sigma width of the optical point spread function (PSF) in ground coordinates, scaled to account for pixel stretch at off-nadir viewing angles:

$$a = \sigma_{\mathrm{psf}} \frac{r_s\, p_{\mathrm{pix}}}{f \cos\theta_z}, \tag{8}$$

where σ_{psf} is the standard deviation of the optical PSF in pixels, r_s is the slant distance from satellite to ground target, p_{pix} is the pixel pitch, f is the focal length, and θ_z is the off-nadir viewing angle.

Finally, the retrieval noise n used in the PoD model is the standard error of the retrieved methane column density – also known as the column precision – averaged within a 500-meter radius of the release point. To formally define the column precision, we follow Rodgers (2000) and express the problem of inferring a state vector of atmospheric and instrument parameters $\boldsymbol{x}$ which we seek to estimate from a vector of measurements $\boldsymbol{y}$ (light irradiance within the passband of the instrument) via the equation

$$\boldsymbol{y} = \boldsymbol{F}(\boldsymbol{x}) + \hat{\boldsymbol{\epsilon}}, \tag{9}$$

where $\boldsymbol{F}(\boldsymbol{x})$ is a nonlinear forward model which describes light propagation in a given state, and $\hat{\boldsymbol{\epsilon}}$ is the vector of errors (residuals) which is the sum of measurement noise $\boldsymbol{\epsilon}_y$ and imperfections of the forward model $\boldsymbol{\epsilon}_F$. We infer the state vector's best estimate $\hat{\boldsymbol{x}}$ via nonlinear optimization, minimizing a cost function that is the sum of squared residuals, weighted by the measurement uncertainty

$$\chi^2(\boldsymbol{x}) = \hat{\boldsymbol{\epsilon}}^T \mathbf{W} \hat{\boldsymbol{\epsilon}}, \tag{10}$$

where $\mathbf{W} = \mathbf{S}_{y,\mathrm{m}}^{-1}$ is the inverse of the measurement covariance matrix, estimated from known variances of photocurrent shot noise σ_{psn}^2, dark current shot noise σ_{dsn}^2, and camera read noise σ_{rn}^2

$$\mathbf{S}_{y,\mathrm{m}} = \mathrm{diag}\left(\sigma_{\mathrm{psn}}^2 + \sigma_{\mathrm{dsn}}^2 + \sigma_{\mathrm{rn}}^2\right). \tag{11}$$

The subscript m in $\mathbf{S}_{y,\mathrm{m}}$ stands for "model", indicating that it is derived from physical modelling prior to performing the inversion. An alternative estimate of the parameter covariance matrix can be formulated based on the residuals of the regression (identified by the subscript r):

$$\mathbf{S}_{y,\mathrm{r}} = \frac{1}{m-n}\frac{\hat{\boldsymbol{\epsilon}}^T\mathbf{W}\hat{\boldsymbol{\epsilon}}}{\mathrm{Tr}(\mathbf{W})/m}\mathbf{I}. \tag{12}$$

Error estimates in measurement space can be converted to state space via the equation

$$\hat{\mathbf{S}}_{x,r} = (\mathbf{K}^T\mathbf{W}\mathbf{K})^{-1}\mathbf{K}^T\mathbf{W}\mathbf{S}_{y,r}\mathbf{W}^T\mathbf{K}(\mathbf{K}^T\mathbf{W}\mathbf{K})^{-1}, \tag{13}$$

where $\mathbf{K} = \frac{\partial \boldsymbol{F}(\hat{\boldsymbol{x}})}{\partial \boldsymbol{x}}$ is the Jacobian matrix of the forward model around the solution $\hat{\boldsymbol{x}}$. Specifically, the standard error on the column density is the diagonal component of the covariance matrix corresponding to the column density.

We note that the standard error based on the fit residuals provides a more accurate and conservative estimate of the local column precision than its "model noise" counterpart which simply propagates sensor shot noise and readout noise into retrieval parameter space and therefore yields only a lower bound that can be exceeded due to correlated noise and poor model fit. Another approach to estimate the noise is to calculate the local standard deviation of the column density within a radius of the origin (Ramier et al., 2023). While this approach is in principle more robust to correlated noise, it requires that all variation within the region of interest be attributable to noise alone, and is therefore not applicable in the presence of an actual methane plume, such as in the context of controlled releases. We therefore select the residuals-derived noise definition for the purpose of modeling the detection performance.

3.1.2 Predictor functions

In addition to providing the set of key driving variables, we use the Jacob heuristic as a template to define candidates for the predictor function $Z(\boldsymbol{X};\boldsymbol{\phi})$, which are listed in Table 2 alongside the associated vector of fitted parameters $\boldsymbol{\phi}$. The candidates were constructed to address one key limitation of the heuristic, which is that even at an average wind speed of zero, there should still be some amount of methane dissipation due to diffusion and small-scale eddies. This implies that the concentration does not diverge to infinity and the PoD remains less than 1 as u approaches zero. We model this by replacing the plain wind speed u in the heuristic by a function $u_d^*(u;\boldsymbol{\phi})$, such that

$$Z(\boldsymbol{X};\boldsymbol{\phi}) = \frac{q}{u_d^*(u;\boldsymbol{\phi})\, n\, a}. \tag{14}$$

We further require the function u_d^* to have dimensions of a speed (length over time), which retains the interpretation of $Z(\boldsymbol{X};\boldsymbol{\phi})$ as a dimensionless SNR-like quantity. It follows that u_d^* can be interpreted as a "detection" effective wind speed, which is analogous but distinct from the "quantification" effective wind speed of the IME method (Eq. 3).

We evaluate 4 predictor functions that follow this general form: (1) the ordinary Jacob heuristic, (2) a linear wind offset, which is the simplest extension, (3) a wind offset added in quadrature, which recovers the ordinary heuristic in the limit of high wind speed, and (4) an effective wind function following the mean of a Rice-distributed variable. The Rice model is motivated by representing the estimated two-dimensional wind vector, $\hat{\boldsymbol{u}} = (\hat{U}, \hat{V})$, as

$$\hat{\boldsymbol{u}} = \boldsymbol{u} + \boldsymbol{\epsilon}_u, \tag{15}$$

where $\boldsymbol{u} = (U, V)$ is the effective wind vector experienced by the plume and $\boldsymbol{\epsilon}_u = (\epsilon_U, \epsilon_V)$ represents measurement error. Under the assumption that ϵ_U and ϵ_V are independent and normally distributed with standard deviation s_u, the magnitude of the wind vector u follows a Rice distribution with parameters $\nu = \hat{u}$ and $\sigma = s_u$. Its mean is positive even when the nominal wind vector is zero, capturing the expectation that unresolved vector variability produces non-zero effective transport at low reported wind speed.

Table 2. Predictor functions and associated parameters

Model name	Equation	Parameters
Jacob heuristic	$Z(\boldsymbol{X}) = \frac{q}{u\, n\, a}$ $u_d^* = u$	$\boldsymbol{X} \subseteq \{q, u, n, a\}$ $\boldsymbol{\phi} = \{\,\}$
Linear wind offset	$Z(\boldsymbol{X}; \boldsymbol{\phi}) = \frac{q}{(u + u_0)\, n\, a}$ $u_d^* = u + u_0$	$\boldsymbol{X} = \{q, u, n, a\}$ $\boldsymbol{\phi} = \{u_0\}$ u_0: wind speed offset (m s^{-1})
Quadrature wind offset	$Z(\boldsymbol{X}; \boldsymbol{\phi}) = \frac{q}{\sqrt{u^2 + u_0^2}\, n\, a}$ $u_d^* = \sqrt{u^2 + u_0^2}$	$\boldsymbol{X} = \{q, u, n, a\}$ $\boldsymbol{\phi} = \{u_0\}$ u_0: wind speed offset (m s^{-1})
Rice-distributed wind	$Z(\boldsymbol{X}; \boldsymbol{\phi}) = \frac{q}{E_{\text{Rice}}[u \mid s_u]\, n\, a}$ $u_d^* = E_{\text{Rice}}[u \mid s_u] = s_u \sqrt{\frac{\pi}{2}} L_{1/2}\left(-\frac{u^2}{2\, s_u^2}\right)$	$\boldsymbol{X} = \{q, u, n, a\}$ $\boldsymbol{\phi} = \{s_u\}$ s_u: uncertainty of wind vector components (m s^{-1}) $L_{1/2}$: Laguerre polynomial of order ½

3.1.3 Inverse link functions

The inverse-link functions considered are defined in Table 3. Because the predictor $Z(\boldsymbol{X}; \boldsymbol{\phi})$ is a positive, signal-to-noise-like quantity, we restrict the inverse-link functions to cumulative distribution functions with support on the positive real line. This choice excludes consideration of models that would predict a non-zero PoD for negative source rates which are unphysical, such as the commonly used logistic and probit inverse link functions. We instead consider their logarithmic counterpart: the log-normal and log-logistic cumulative distribution functions (CDF).

Table 3. Inverse-link functions and associated parameters

Model name	Equation	Parameters
Log-normal	$P(Z;\theta) = \frac{1}{2}\left(1 + \mathrm{erf}\left(\frac{\ln Z - \mu}{\sqrt{2}\,\sigma}\right)\right)$	$\boldsymbol{\theta} = \{\mu, \sigma\}$ μ: mean of ln(Z) σ: standard deviation of ln(Z)
Log-logistic	$P(Z;\theta) = \frac{1}{1 + e^{\mu/s} Z^{-1/s}}$	$\boldsymbol{\theta} = \{\mu, s\}$ μ: mean of ln(Z) s: scale

3.2 Experimental results and model regression

The dataset used to analyze detection capability includes 125 samples: 94 TP (detections) and 31 FN (misses), about equally split between single-blind (62) and pseudo-blind (63). Experimental results and fitted regressions are presented graphically in Fig. 3 as functions of the metered methane emission rate (1st column of subplots), the value of the SNR-like predictor function (2nd column), and in a 2-dimensional space with emission rate on the *y* axis and wind speed on the *x* axis (3rd column). Due to the large number of possible combinations of link functions, predictor functions, and environmental variable subsets, we selected two models for plotting: the heuristic predictor (first row), and linear wind offset (second row), both using the full set of environmental variables $\{q, u, n, a\}$ and a log-normal inverse link function. Optimized model parameters and derived detection limits for an extended list of models is provided in Table 4. Additionally, an analysis comparing the quality of model candidates in terms the Akaike and Bayesian information criteria will be presented in section 3.3, supporting the choice of the log-normal linear-offset PoD function as primary model.

Table 4. Detection model parameters and derived detection limits for various predictor functions and inverse-link function. Values are the results of maximum likelihood optimization and uncertainties are the standard deviation of the bootstrap ensemble. Detection limits are evaluated at u = 3 m s^{-1}, n = 7.0 mmol m^{-2}, a = 27.0 m.

Predictor	Link	μ	σ	u_0 (m s^{-1})	Z_{50}	Q_{50} (kg h^{-1})	Q_{90} (kg h^{-1})
Heuristic	Log-normal	1.061 ± 0.071	0.373 ± 0.068		2.89 ± 0.20	94.6 ± 6.7	152.7 ± 15.0
Heuristic	Log-logistic	1.060 ± 0.089	0.214 ± 0.051		2.89 ± 0.24	94.5 ± 7.8	151.2 ± 19.2
Linear	Log-normal	0.540 ± 0.248	0.267 ± 0.050	2.289 ± 1.694	1.72 ± 0.39	99.0 ± 5.3	139.3 ± 11.1
Linear	Log-logistic	0.551 ± 0.266	0.155 ± 0.031	2.197 ± 1.858	1.73 ± 0.42	98.4 ± 5.5	138.3 ± 11.5
Quadrature	Log-normal	0.819 ± 0.152	0.275 ± 0.052	2.499 ± 1.099	2.27 ± 0.32	96.6 ± 5.4	137.6 ± 11.0
Quadrature	Log-logistic	0.826 ± 0.165	0.160 ± 0.033	2.423 ± 1.142	2.28 ± 0.35	96.1 ± 6.2	136.8 ± 11.3
Rice	Log-normal	0.851 ± 0.183	0.278 ± 0.095	2.003 ± 0.957	2.34 ± 0.39	95.9 ± 5.5	137.0 ± 10.8
Rice	Log-logistic	0.858 ± 0.169	0.162 ± 0.036	1.948 ± 0.873	2.36 ± 0.41	95.5 ± 6.4	136.2 ± 11.3

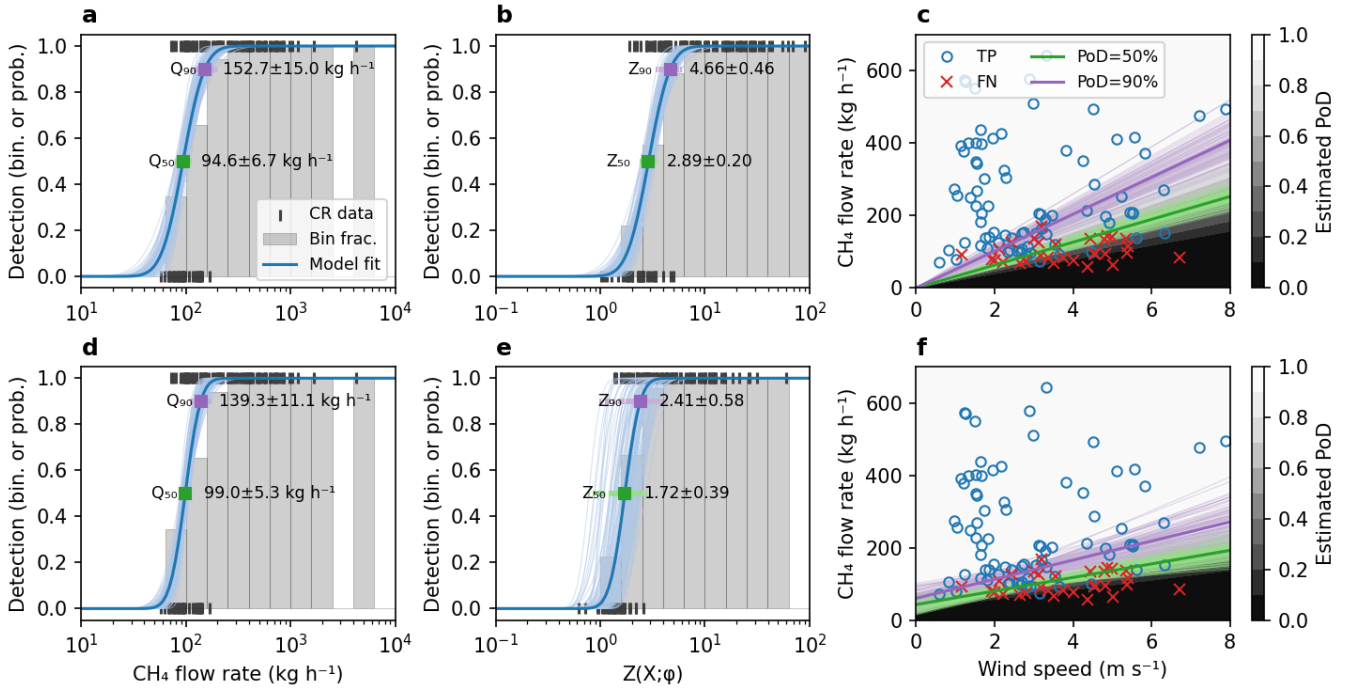

Figure 3. Detection results and fitted probability of detection for two candidate models: (a-c) heuristic, (d-f) linear wind offset. The detections and PoD are plotted as a function of the emission rate (1st column), the SNR predictor value (2nd column), and as a 2D function of emission rate and wind speed (3rd column). Binary results of controlled releases are shown as discrete markers: black vertical ticks, and blue (TP) or red (FN) markers. Histogram bars represent the detection fraction in each corresponding bins. Continuous curves represent the fitted PoD model – thick ones for the maximum likelihood solution and thin ones for the bootstrap uncertainty evaluation. The detection limit at specific PoD of 50% and 90% are highlighted in green and purple respectively, with associated text labels providing the maximum likelihood estimate and 1-sigma uncertainty derived from bootstrapping.

The detection limit at specified PoD corresponds to contours of $P\left(Z\left(\boldsymbol{X};\widehat{\boldsymbol{\phi}}\right);\widehat{\boldsymbol{\theta}}\right)$ and can be expressed explicitly by solving Eq. (4) for the emission rate:

$$Q_p = Z_p(p;\hat{\mu},\hat{\sigma})\; u_d^*(u;\hat{u}_0)\; n\; a, \tag{16}$$

where Q_p is the emission rate detected with probability p (typically 50% or 90%), $Z_p(p;\hat{\mu},\hat{\sigma})$ is the quantile function of the lognormal SNR predictor, and the circumflex indicates best-fit estimates of the model parameters $\{\hat{\mu},\hat{\sigma},\hat{u}_0\}$. We evaluate the uncertainty of the fitted detection models and all derived parameters using the bootstrapping method (1000 random trials). This method is used to derive uncertainty bounds on fitted model coefficients (μ,σ,u_0), as well as other derived quantities such as detection limits.

The detection limits Q_{50} and Q_{90} are shown in Fig. 3 as square markers (1D subplots) and continuous contour lines (2D subplots of q and u). In particular, specifying PoD = 50% and median conditions as reference (wind speed u = 3 m s^{-1}, noise

n = 7.0 mmol m^{-2}, and spatial resolution a = 27.0 m), we find the value of Q_{50} to be highly consistent between the models listed in Table 4, ranging between 94.5 ± 7.8 kg h^{-1} (heuristic, log-logistic) and 99.0 ± 5.3 kg h^{-1} (linear wind offset, log-normal).

The detection limit can also be expressed directly in terms of the SNR predictor, with values of Z_{50} ranging between 1.72 (linear wind offset, log-normal) and 2.89 (heuristic, log-normal). Note that we observe more jitter of the bootstrap curves when plotting the PoD against Z_p compared to Q_p. This is because the predictor includes a fitted parameter u_0 which has some level of degeneracy with parameters of the inverse-link functions, particularly the offset term μ. In Q space, error on u_0 are compensated by errors on m while maintaining a similar derived Q_p, while Z_p does not have that compensation. Because the heuristic model does not have any free predictor function parameters, the jitter on Z_p curves is the same as that of Q_p. Still, in every case, the numerical values are physically realistic considering the interpretation as a SNR, which suggests that a Z_p value around 2 is needed to achieve 50% PoD, and around 3 – 4 for 90% PoD.

3.3 Comparison of detection model variants

The preceding analysis used representative model configurations to illustrate the estimated probability-of-detection behavior. Here, we expand the analysis to compare alternative choices of predictor variables, predictor functions, and inverse-link functions. We first examine the impact of the driving variables $\{q, u, n, a\}$ in Fig. 4 (a-d) by varying the subset of variables while fixing the predictor and inverse-link functions to heuristic and log-normal, respectively. The second row of subfigures Fig. 4 (e-h) examines the various combinations of predictor and inverse-link functions (e-h). For each case we evaluate Q_{50} to provide an indication of its consistency and robustness to choice of model, as well as the corresponding transition width $\Delta Q_{80} = Q_{90} - Q_{10}$. Following (Conrad et al., 2023; Thorpe et al., 2024), we use the Akaike information criterion with small-sample correction (AICc) as a metric of fit quality that penalizes overfitting due to excessive parametrization:

$$\mathrm{AICc} = -2\ln\hat{\mathcal{L}} + 2k + \frac{2k(k+1)}{N-k-1}, \tag{17}$$

where k is the number of fitted model parameters, N is the number of samples, and $\hat{\mathcal{L}}$ is the value of the likelihood function at the solution (maximum likelihood). We also compute the Bayesian information criterion (BIC):

$$\mathrm{BIC} = -2\ln\hat{\mathcal{L}} + k\ln N\,, \tag{18}$$

as an alternative measure of goodness of fit.

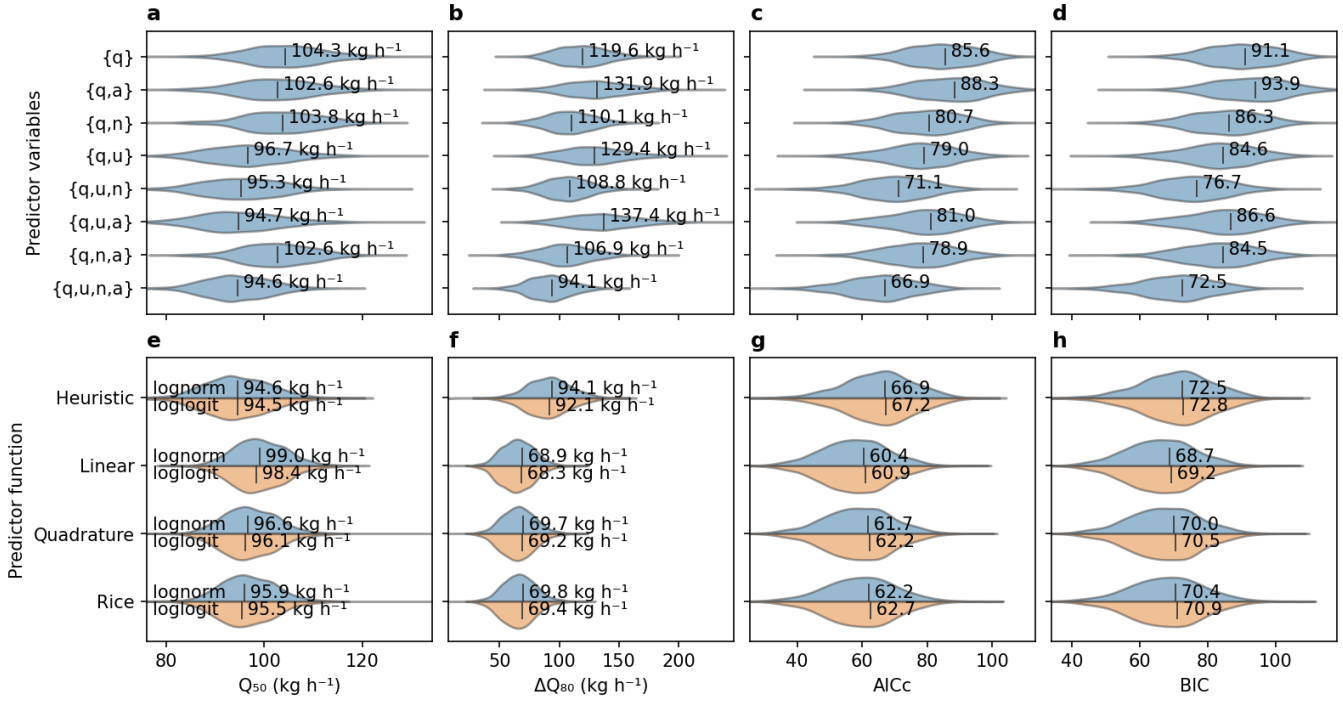

Figure 4. Evaluation and comparison of detection model candidates in terms of (a,e) 50% detection limit, (b,f) 10% to 90% transition width, (c,g) Akaike information criterion, and (d,h) Bayesian information criterion. Top panels (a-d) compare subsets of the driving variables {*q*,*u*,*n*,*a*} with the predictor and link functions set to Jacob heuristic and log-normal. Bottom panels (e-h) compare combinations of predictor function (y-axis) and inverse-link function (log-normal in blue, log-logistic in orange), using the full set of driving variables. Values for the maximum likelihood solution using all samples are labelled textually and noted by a vertical bar, while colored envelopes represent the distribution of values across the 1000 bootstrap subsets.

Comparing choices of predictor variables, we observe clear variability in model quality, the best models (lowest AICc and BIC) being ones that use all 4 parameters. Examining the 2- and 3-variables subsets provide interesting insights to their relative influence: there is a clear reduction of AICc and BIC when adding the wind speed (u) or noise (n). Adding spatial resolution (a) by itself does not help as the $\{q,a\}$, $\{q,n,a\}$ and $\{q,u,a\}$ combinations perform worse than their resolution-free counterparts. However, including the resolution along with the other variables (such as $\{q,u,n,a\}$ vs $\{q,u,n\}$) improves the model quality, supporting that a should be included in the PoD model. Overall, our analysis of parameters suggests that over the range of operational conditions, q, u and n are the main drivers, while resolution varies little across nominal operating conditions and thus has a less pronounced effect.

Examining the various combinations of predictor and inverse-link functions in Fig. 4 (e-h), we first highlight that the differences between models are small compared with the bootstrap uncertainty ranges. Those provide an indication of the sensitivity of the results to perturbations of experimental sample set, showing that the rankings obtained here could be swayed one way or another as more samples will be added in the upcoming years. One conclusion is that the plain Jacob heuristic has the highest transition width, AICc, and BIC, supporting the introduction of a wind offset parameter in one form or another. Of the 3 remaining predictor forms, the linear wind offset results in the lowest information scores, albeit by a small margin

compared with quadrature and Rice models. Regarding the choice of inverse-link function, we observe that a log-normal model modestly but systematically outperformed the log-logistic.

Based on those results, we adopt the log-normal inverse-link function with linear wind offset predictor, driven by all four variables (q, u, n, a), as the primary model for the remainder of this paper. We highlight that the detection limits and transition widths derived from various models in Fig. 4 (e) are highly consistent, supporting the robustness of derived performance metrics to the choice of model.

3.4 Convergence and applicability of the detection performance

The analysis presented in Fig. 5 examines the evolution and applicability of the detection model between 2021 and 2026 as the GHGSat constellation grew with new instruments, as the data processing toolchain was upgraded, and as more single-blind samples from the Stanford study became available. The total number of controlled release events prior to a given date is shown in Fig. 5 (a), which highlights TP (blue) and FN (red), as well as the self-organized or blind attribute of the experiments. The larger increases are mainly driven by the GHGSat/CMC campaigns of 2022 and 2023, as well as the Stanford year-long 2025 study (Brandt et al., 2026).

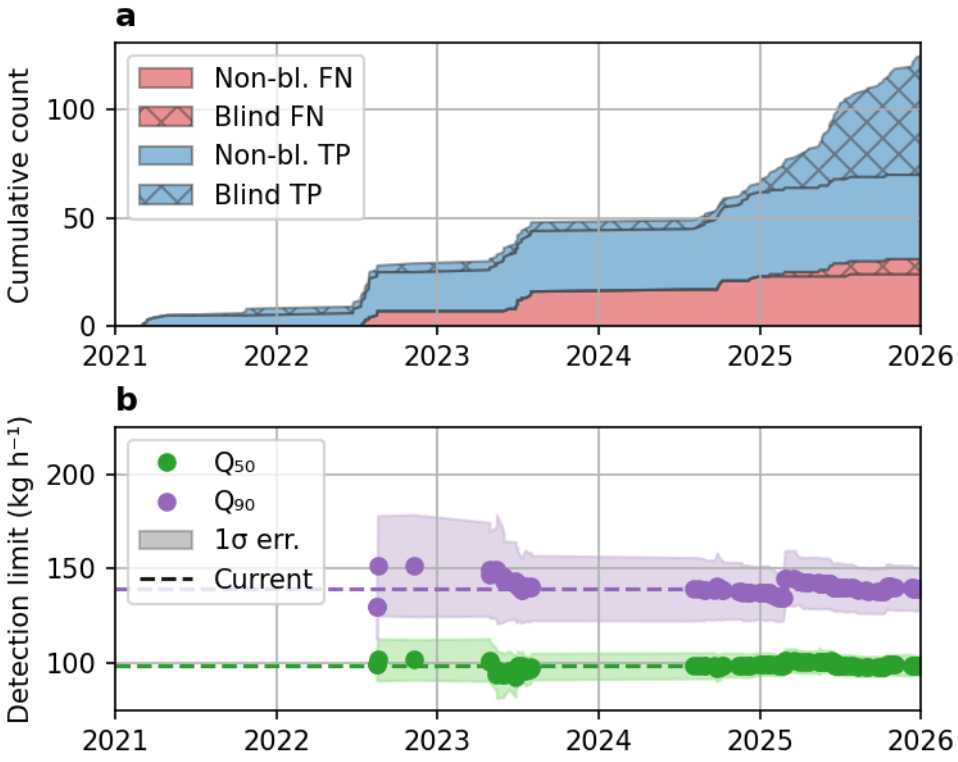

Figure 5. Convergence of the detection limits with the increase of the number of samples between 2021 and 2026. (a) Number of controlled release events accumulated over time, classified as true positive (TP, blue) or false negative (FN, red) and as self-organized (flat) or single-blind (patterned). (b) Detection limits (markers) and associated uncertainties (shaded regions) at PoD = 50% and

90%, based on prior controlled release events. Dashed lines represent the current estimate based on all available samples as of May 2026.

Figure 5 (b) shows the corresponding evolution of the detection limit (evaluated at 50% and 90% PoD and $u = 3$ m s^{-1}, using the linear wind offset predictor) based on samples available up to the date on the x-axis. Note that the detection limits are only evaluated starting mid-2022 as the first missed detections (FN) make the analysis possible. After some initial fluctuations, the series converges to the current values $Q_{50} = 99.0$ and $Q_{90} = 139.3 \pm 11.1$ kg h^{-1} as the number of samples increases. The associated uncertainties, shown as shaded regions, also reduce over time, as expected from the increasing sample size. The addition of a large set of single-blind samples in 2025 did not affect the estimated performance metrics significantly, providing stable convergence of Q_{50} and a modest improvement of Q_{90}. This supports the assumption that the pseudo-blind GHGSat-organized releases, while not truly independent, were treated in a consistent way and are valid inclusions for this analysis.

4 Quantification accuracy

Controlled releases allow us to assess the accuracy of GHGSat's estimated emission rates by comparing them against the "true" rate measured by the flowmeter on the ground. We base our analysis on the same multi-campaign dataset described in Tab. 1 and used in the detection limit analysis, restricted to emissions that were successfully detected (true positives) – no rate estimate is performed for undetected plumes. A minor difference from the detection analysis is that the quantification dataset excludes two observations submitted as "detected but not quantified" – one from phase 3 of the Stanford 2025 study and one from the GHGSat/CMC subset – in which the concentration retrieval field was significantly corrupted at the plume location by retrieval artifacts or high cirrus cloud coverage, yet an emission could still be discerned. The quantification analysis is therefore based on a set of 92 true positive samples out of the 94.

The comparison between the metered and estimated source rates is shown in Fig. 6 using 3 different scales and/or variables: (a, d) parity charts in linear scale, (b, e) parity charts comparing the logarithm of the metered and estimated rates, and (c, f) the log of the estimated/metered error ratio as a function of the metered rate. In all panels, markers indicating individual TP samples are colored depending on the type of blinding of the experiment (pseudo-blind in blue or single-blind in orange), and ordinary least squares (OLS) regression lines are included for each type as well as for the full dataset (black). A dashed grey line indicates the ideal outcome (estimated equals metered) for visual reference. The first row of subplots (a–c) shows the "reported" rates based on model wind; the second row (d–f) shows the corresponding estimates using wind from a local anemometer. Using reported winds preserves strict blindness of third-party experiments and ensures consistency with published datasets. For multi-phase campaigns in which a source-rate estimate was delivered to the third party both before and after local wind speeds were revealed (Stanford 2021 and 2022), we report the estimates made without local wind information, which are representative of standard commercial processing.

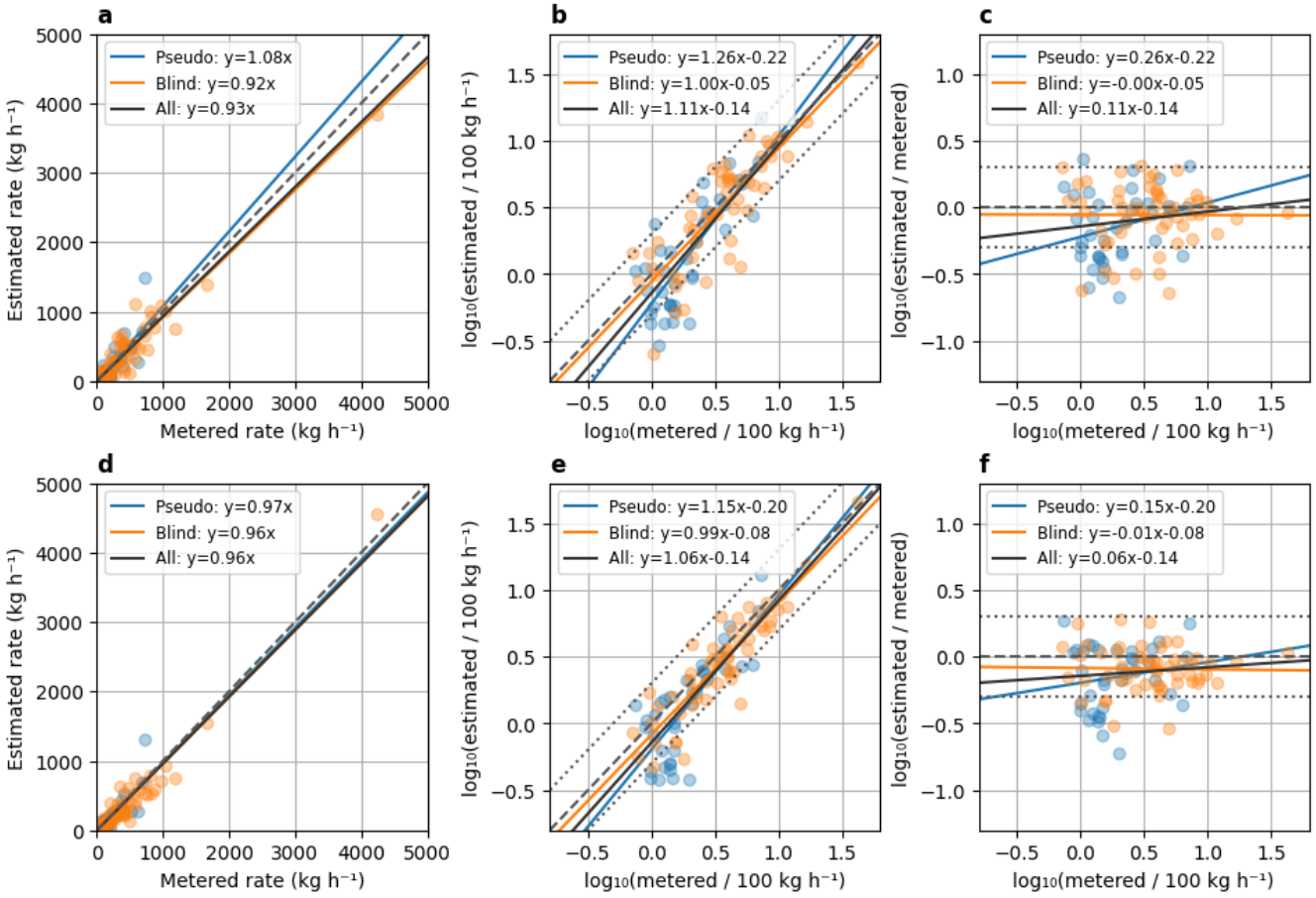

Figure 6. Accuracy of the estimated flow rates (using weather model and local anemometer wind speed) compared with ground measurements, represented as (a,d) linear scale parity chart, (b,e) logarithmic scale parity chart, and (c,f) logarithmic error ratio as a function of the logarithm of the metered rate. Data samples and ordinary least squares regressions are shown from pseudo-blind tests (blue), single-blind tests (orange), and all samples combined (black). The dashed grey line represents the parity (1:1) line and the dotted grey lines are the margins for 2× under or overestimation.

Estimated and metered rates agree well overall. With as-reported rates across all true positives, the linear OLS regression has a slope of 0.93 ± 0.03 (standard error on the slope) and a coefficient of determination $R^2 = 0.92$. Substituting a local anemometer wind yields a modest improvement in the regression (slope = 0.96 ± 0.02, $R^2 = 0.95$) and a clear reduction in scatter around the parity line, confirming the importance of accurate wind measurements for emission quantification.

One limitation of using a linear scale to assess quantification accuracy is that the linear regression slope is largely determined by the samples with high emission rates. The logarithmic parity chart and error-ratio plot provide clearer visualization at small emission rates. These visualizations reveal a broader scatter and a tendency to underestimate the true rate for the small plumes (relative to the ~100 kg h^{-1} detection limit), whereas errors for large plumes are more narrowly distributed and more symmetric around the parity line. The following section further investigates this finding and proposes correction strategies to obtain unbiased estimates independently of the emission rate.

4.1 Approaches for emission-rate estimate bias correction

The controlled-release results presented in Fig. 6 (e-f) showed that a subset of emission-rate estimates, concentrated among the smaller sources, were biased low. Because the concentration enhancement from plumes in the ~100 kg h^{-1} range becomes small relative not only to random noise but also to any systematic bias (e.g., correlated artifacts), a bias in the L2 retrieval is therefore likely to affect small plumes disproportionately. To mitigate this effect while providing evidence to support the L2 bias hypothesis, we implement a local background correction (BGC) that estimates the baseline concentration in the immediate vicinity of each plume by averaging the retrieved concentration over pixels lying more than 3 and fewer than 13 pixels away from any pixel in the plume mask (implemented using morphological dilations with a square structuring element), forming a ~300 m wide annular region around the plume (Fig. 7a). The 3-pixel buffer region between the plume and background masks avoids the inclusion of diffuse CH_4 enhancements below the masking threshold.

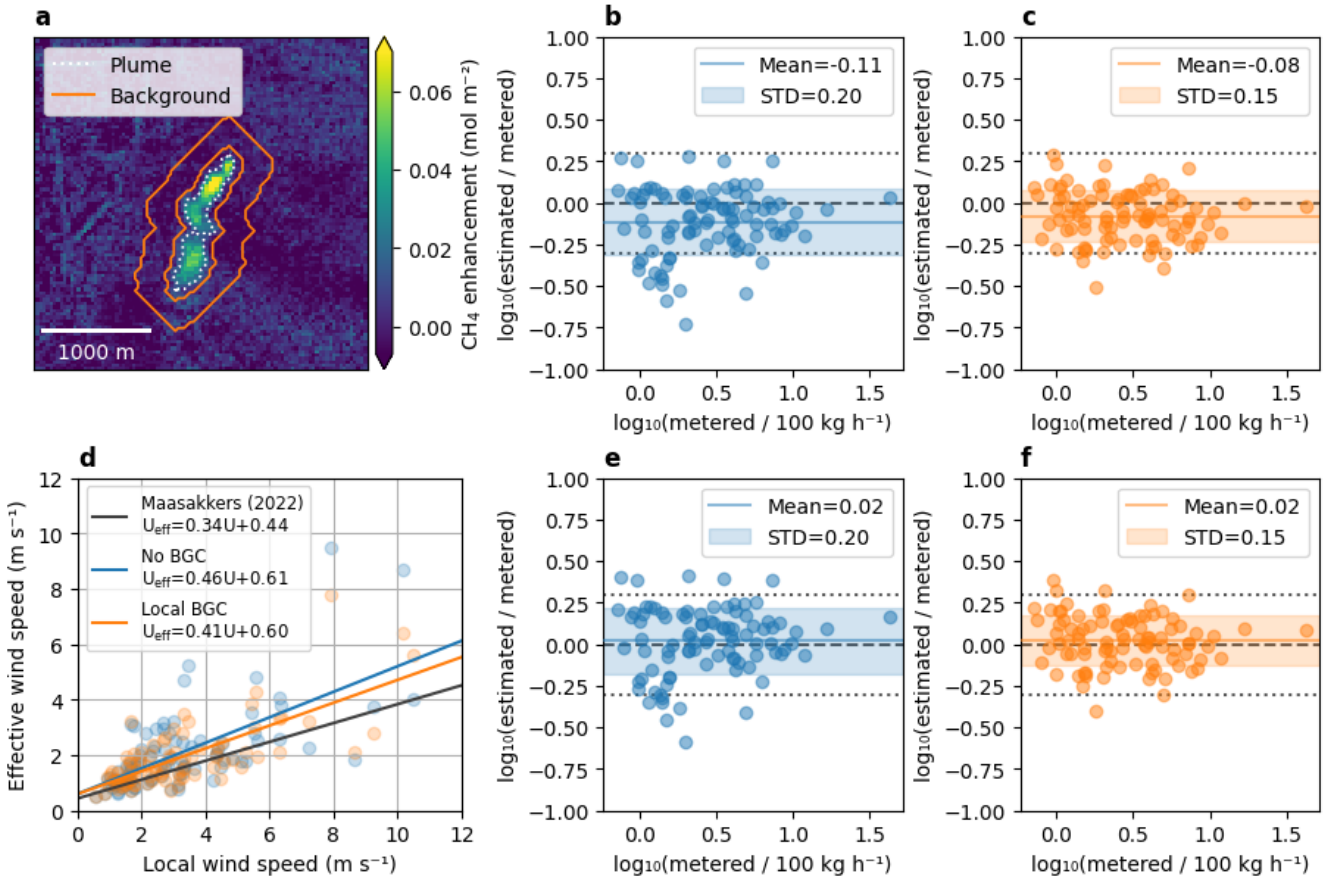

Figure 7. Emission rate bias correction. (a) Illustration of the method for local background correction (BGC) by expanding the plume mask (dotted white line) to generate a padded perimeter (orange line) within which the background concentration is calculated. (b,c,e,f) Logarithmic quantification error ratio for (b) No local BGC, original U_{eff}; (c) Local BGC, original U_{eff}; (e) No local BGC, updated U_{eff}; (f) Local BGC, updated U_{eff}. (d) Empirical calibration of the effective wind speed.

The correction is applied to the column density enhancements Ω contained within plume mask M_P, by subtracting the mean column density enhancement within the background mask M_{BG}:

$$\mathrm{IME} = A_{\mathrm{gc}} \sum_{i \in M_P} (\Omega_i - \overline{\Omega}_{\mathrm{BG}}), \tag{19}$$

$$\overline{\Omega}_{\mathrm{BG}} = \frac{1}{N_{\mathrm{BG}}} \sum_{i \in \mathrm{M_{BG}}} \Omega_i, \tag{20}$$

where A_{gc} is the area of a ground cell and N_{BG} is the number of ground cells in the background mask. Applied on its own, this correction markedly mitigates the low-bias outliers among small sources, which can be observed by comparing Fig. 7b (no BGC applied) with Fig. 7c (local BGC applied). The correction reduced both the overall scatter (standard deviation of the logarithmic error ratio from 0.20 to 0.15) and the global bias (mean of the logarithmic error ratio from –0.11 to –0.08). Note that in this analysis, source rates were estimated using local wind speed from anemometers to better highlight the effects of the corrections from the high uncertainty of model wind speed.

The small bias that remains after BGC can always be further compensated by applying a global scaling to the estimated source rates. A natural way to implement this correction when using the IME method is to update the effective wind speed calibration. This calibration was originally tuned from numerical simulation (Maasakkers et al., 2022; Varon et al., 2018), but it can instead be derived empirically from the controlled-release results. For each release we define a "true" effective wind speed as the value of U_{eff} that would reproduce the metered source rate q from the measured integrated mass enhancement (IME) and plume length:

$$U_{\mathrm{eff,true}} = \frac{q\, L_{\mathrm{eff}}}{\mathrm{IME}}. \tag{21}$$

We then plot $U_{\mathrm{eff,true}}$ against the local wind speed and fit an ordinary-least-squares linear regression (Fig. 7d). The resulting linear equation $U_{\mathrm{eff}} = 0.41\, u + 0.60$ is then used as an empirical effective wind speed in the IME method, in place of the numerically calibrated model expressed in Eq. (3).

Combining both corrections – local BGC together with the recalibrated effective wind speed – removes most of the residual global bias: the mean of the logarithmic error ratio rises from –0.11 (Fig. 7b) to +0.02 (Fig. 7f), while the scatter is held at the reduced level of 0.15 (standard deviation of the logarithmic error ratio). We note that the effective wind speed recalibration could also be done independently of the local background correction (Fig. 7e). This standalone version is equivalently effective at removing the global bias, but does not address the small rate outliers or reduce the magnitude of the scatter.

Taken together, the local background correction and the empirically recalibrated effective wind speed constitute a straightforward refinement of the quantification chain that improves accuracy across a wider range of emission rates, recovering the low-rate sources that were previously underestimated without degrading performance at higher rates. Although demonstrated here on GHGSat retrievals, neither correction relies on instrument-specific assumptions, and could therefore be transferable to other point-source imaging systems facing similar biases.

4.2 Comparison of wind sources

Wind speed is a key parameter in source rate estimation and a major contributor to its uncertainty budget (Varon et al., 2018). Many weather forecast and reanalysis models are available as potential wind data sources, but their coverage may be restricted to certain geographic areas, and the latency before data becomes available can also constrain the choice for a measurement provider with operational delivery requirements. GHGSat uses OpenWeather, a third-party aggregator that combines data from multiple weather models, as its primary wind source. While the majority of the releases included in this study were performed in North America, the input models available to the aggregator may vary regionally. To evaluate the robustness of quantification to the choice of wind data, we compare in Fig. 8 the emission-rate estimates from three widely used models: ECMWF reanalysis fifth generation (ERA5, a global reanalysis), ECMWF Integrated Forecasting System (IFS, a global forecast), and NOAA High-Resolution Rapid Refresh (HRRR, a regional forecast covering the continental United States and a portion of Canada that includes the Brooks release site). We also include estimates from a co-located anemometer as a reference. Note that results presented in Fig. 8 do not include the bias correction scheme proposed in the previous section, since the effective wind recalibration would be applied individually for each wind source and result in unbiased estimates for all cases.

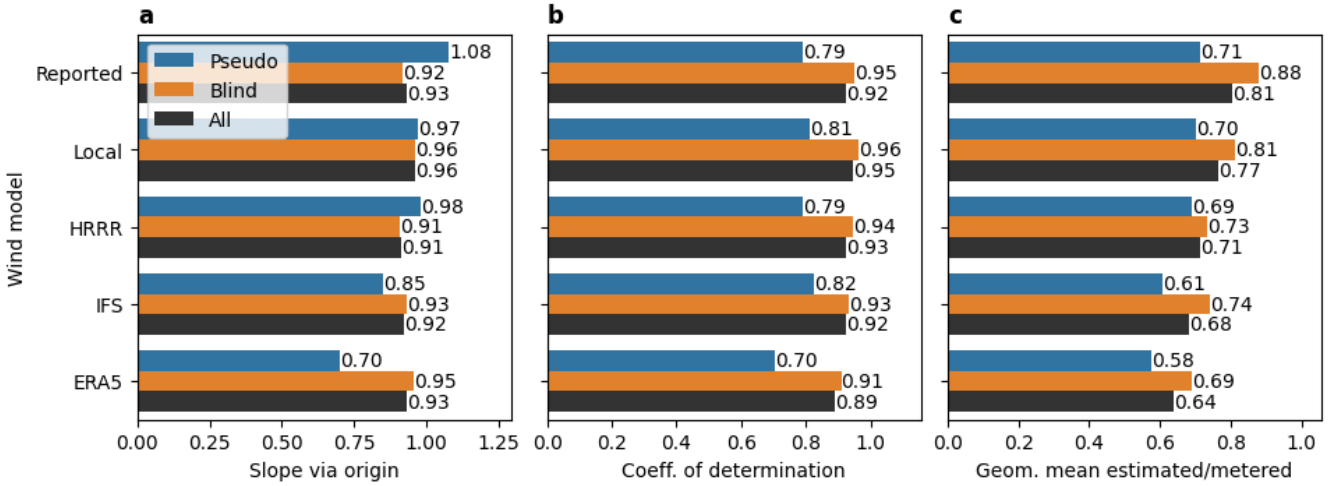

Figure 8. Regression statistics for estimated versus metered source rates under five wind data sources (as-reported, local anemometer, HRRR, IFS, and ERA5): (a) OLS slope through the origin, (b) coefficient of determination R^2, and (c) root-mean-square of the logarithmic error ratio. Bar colors distinguish all true positives (black), pseudo-blind (blue), and single-blind (orange) subsets. Values nearer 1 indicate closer agreement with the metered rate.

When aggregated across all true positives, the four model-derived wind sources yield broadly comparable performance: OLS slopes through the origin fall in a narrow 0.91–0.93 range and R^2 values lie between 0.86 (ERA5) and 0.89 (IFS and HRRR), essentially indistinguishable from the as-reported baseline (slope = 0.93, R^2 = 0.88). This insensitivity to the choice of reanalysis or forecast model is a desirable robustness property for operational quantification, since it indicates that emission

rate estimates do not depend strongly on the specific wind product available at a given location or latency. As previously discussed, substituting the local anemometer wind raises the slope to 0.96 and R^2 to 0.92.

The geometric mean of the estimated-to-metered ratio (Fig. 8c) provides a complementary view that is less sensitive to a few high-rate samples than the linear OLS slope. All five wind sources produce geometric means below unity (0.64–0.77 without bias correction across the full dataset). The local anemometer again performs best (0.77), while ERA5 shows the largest negative bias (0.64). The magnitude of the bias appears correlated with the spatial resolution of the weather model: 3 km HRRR is least biased, followed by 9 km IFS, while ERA5 (~30 km, 0.25°) shows the largest negative bias. We attribute this trend to spatiotemporal averaging of the wind transport: sub-grid wind speeds resemble a random walk in which instantaneous local speeds exceed the average drift of the center of mass. This averaging effect being dependent on the grid size, coarser resolution models lead to more underestimation of the local wind.

In summary, this analysis supports that GHGSat's quantification accuracy is robust to the choice among major operationally available wind products – an important property for global deployment, where HRRR-class regional models are not available. A co-located anemometer, if available, measurably improves quantification, but the aggregate gain over global model winds is small. Finally, small differences between models may be driven by their different spatial resolution (grid size). This effect is correctible for any wind model by recalibrating the effective wind speed as described in section 4.1.

5 Conclusions and discussion

This study presents a comprehensive controlled-release assessment of the GHGSat constellation's detection and quantification performance, drawing on a multi-campaign dataset spanning 2021 to 2026 that combines self-organized releases with independent third-party experiments. Framing detection as a probabilistic, conditions-dependent process and grounding the predictor in the Jacob heuristic yields a model that is simple enough to be constrained by the available sample size yet retains physical interpretability across the operational range of the constellation.

The analysis supports several conclusions. First, source rate, wind speed, and retrieval noise are the dominant drivers of detection probability over the operational range examined, while spatial resolution varies too little within nominal viewing conditions to register as an independent predictor once the other three are included. Second, the detection performance is highly consistent across model variants, with Q_{50} ranging from 94.6 to 99.0 kg h^{-1} depending on the predictor function. The linear wind offset predictor combined with a lognormal inverse-link had the best fit with the experimental data, in terms of Akaike and Bayesian information criteria. Third, this estimate has converged stably as the sample size has grown, and the addition of a large set of single-blind Stanford samples in 2025 did not significantly shift Q_{50} or Q_{90}, supporting the validity of pooling self-organized and independently blinded releases.

The link function parameters derived here from controlled releases and the associated $Q_{50} \sim 100$ kg h^{-1} differs from the survey-mode detection limit reported by the same group of authors (Jervis et al., 2026), who estimated $Q_{50} \sim 460$ kg h^{-1} by fitting a joint model of the emission rate distribution and detection probability to a large ensemble of detected O&G plumes

from 2024–2025. The approximately 4.5-fold difference is driven by two main factors: differences of observation conditions, which are described explicitly by predictor variables $\boldsymbol{X} = \{q, u, n, a\}$, and differences in inspection conditions, which are described by link functions parameters $\boldsymbol{\theta} = \{\mu, \sigma\}$. Observation conditions encountered in controlled releases are on average slightly more favorable than in global operations with median wind speed 3.2 m s^{-1} and noise 9.9 mmol m^{-2} (compared to 3.0 m s^{-1} and 7.0 mmol m^{-2} in the controlled release dataset). Evaluating the detection model in global median conditions yields Q_{50} = 159.7 kg h^{-1}. Consequently, the observation conditions account for a factor ~1.6 of the performance gap.

The other factor is the difference in inspection conditions and prior information. GHGSat distinguishes two modes of data processing. Target-mode applies to commercially contracted observations, where target site locations are known a priori from customers and visually inspected by GHGSat analysts. Survey-mode applies to other regions of the world surveyed by the constellation where both the existence and location of emitting sites may be unknown. They are pre-screened by artificial intelligence (AI), and the detected emissions are validated by human analysts. This mode is relevant for building global measurement-informed inventories based on the full observation capacity of the constellation. Controlled releases provide an estimate most relevant to target-mode detection performance, as they were both processed directly by GHGSat analysts with approximate knowledge of potential release locations. In contrast, the performance estimated by Jervis et. al (2026) was derived from – and applies to – GHGSat's global catalogue of observations processed in survey-mode.

In summary, the two estimates are not in contradiction but characterize complementary aspects of constellation performance: the controlled-release Q_{50} reported here quantifies the sensitivity achievable under favorable conditions with known source location, while the survey-mode Q_{50} of Jervis et al. (2026) describes the effective detection threshold encountered across the full operational envelope.

On the quantification side, parity analysis across 92 true-positive samples yields an OLS slope of 0.93 and R^2 = 0.88 with reported model winds, improving to 0.96 and 0.92 when a co-located anemometer is substituted. Quantification accuracy is largely insensitive to the choice among the major operationally available wind products (ERA5, IFS, HRRR, and the OpenWeather aggregator) – an important robustness property for global deployment, where regional high-resolution models are not always available. The residual low-rate underestimation is common to all wind sources and correlates with wind-model spatial resolution, pointing to spatiotemporal averaging of sub-grid wind variability as a likely contributor. As a step toward addressing this, we demonstrated a bias correction that combines a local background correction with an empirically recalibrated effective wind speed, reducing both the scatter and the global bias of the quantification and recovering the previously underestimated low-rate sources.

Several limitations qualify the scope of these results and define directions for follow-up work. The controlled releases used here were conducted predominantly at flat, arid, or prairie sites that are representative of many oil and gas production basins but not of typical landfills, coal mines, or urban environments, where surface and meteorological conditions differ substantially. Similarly, controlled release experiments included in this study were all point-source in nature, and extension to area sources such as landfills and open-pit mines will require dedicated methodology and validation campaigns (Hossain et al., 2026).

Additionally, while the dataset robustly constrains constellation-level detection and quantification models, the *per instrument* sample size is not sufficient to constrain independent models that would isolate any manufacturing variability between individual payloads. However, we do not consider this a major limitation. Results should indeed be interpreted as representative of the full GHGSat constellation, and this remains a practical and useful outcome since satellites are tasked indistinctively to any targets in nominal operations. Moreover, instrument-to-instrument variability of the PoD is already accounted for to a large extent, through the noise and resolution predictor variables which are inherently instrument- and observation-specific. The fit parameters u_0, μ and σ, which would be derived from hypothetical per-instrument fits, should in contrast be driven mainly by the data analysis pipeline (inspection conditions) and therefore mostly instrument-independent.

In conclusion, these results establish a transparent, statistically grounded baseline for the detection and quantification performance of the GHGSat constellation. The probabilistic, conditions-dependent formulation may be updated as new controlled releases become available and provides a template and methodology for comparing performance across the broader population of methane point-source imagers.

Data availability

All data required for this study are included in the figures and tables of the article. Data included in the figures may be provided in tabular form upon request.

Author contributions

AR, HD, and JMcK contributed to the conceptualization of the study. Data curation, formal analysis, investigation, and software development were led by AR with support from HD, AD, LF, MG, DJ, DM, JMcK, AM, and ET. AR and HD prepared the original draft of the manuscript. All remaining authors contributed to review and editing.

Competing interests

The authors declare no competing financial interest.

Disclaimer

Copernicus Publications remains neutral with regard to jurisdictional claims made in the text, published maps, institutional affiliations, or any other geographical representation in this paper. While Copernicus Publications makes every effort to include appropriate place names, the final responsibility lies with the authors. Views expressed in the text are those of the authors and do not necessarily reflect the views of the publisher.

Acknowledgements

The authors thank the teams at CMC, Stanford University, TADI, and FluxLab, whose controlled-release campaigns and supporting measurements made this validation possible. We also acknowledge the use of artificial intelligence (AI) for editorial assistance, including drafting and refining text, improving clarity and flow, and checking consistency of terminology and cross-references. All scientific content, data analysis, interpretation of results, and conclusions are the work of the authors, who reviewed and verified all AI-assisted output and take full responsibility for the contents of this paper.

Financial support

The work presented in this paper was carried out as part of the authors' salaried employment; no external funding was received.

Review statement

[The review statement will be added by Copernicus Publications listing the handling editor as well as all contributing referees according to their status anonymous or identified.]

References

Anon: Methane Detection and Quantification Testing Protocol Canada, Carbon Management Canada, 2025.

Bell, C., Rutherford, J., Brandt, A., Sherwin, E., Vaughn, T., and Zimmerle, D.: Single-blind determination of methane detection limits and quantification accuracy using aircraft-based LiDAR, Elementa: Science of the Anthropocene, 10, 00080, https://doi.org/10.1525/elementa.2022.00080, 2022.

Blackmore, D. C., Hickey, J.-P., Wigle, A., Osadetz, K., and Daun, K. J.: A Bayesian technique for quantifying methane emissions using vehicle-mounted sensors with a Gaussian plume model, Atmospheric Environment, 344, 121002, https://doi.org/10.1016/j.atmosenv.2024.121002, 2025.

Bourlon, E., Hossain, R., Buntov, P., Dudak, Y., Risk, D., Farjami, F., Martino, R., Amaral, M., Tarakki, N., Coyle, L., Bailey, A., and Khaleghi, A.: Measurement Data from the FluxLab 2024 and 2025 Controlled Release Campaigns at the Simulation Facility for Landfill Emission Experiments (SIMFLEX) (4.0), https://doi.org/10.5683/SP3/ZYVDC1, 2026.

Brandt, A., Reuland, F., Adams, T., Sherwin, E., Abbadi, S. E., and Kort, E.: Unlocking credible space-based methane sensing through a year-long single-blind test, https://doi.org/10.21203/rs.3.rs-9110475/v1, 22 April 2026.

Bruno, J. H., Jervis, D., Varon, D. J., and Jacob, D. J.: U-Plume: automated algorithm for plume detection and source quantification by satellite point-source imagers, Atmos. Meas. Tech., 17, 2625–2636, https://doi.org/10.5194/amt-17-2625-2024, 2024.

Chen, Z., El Abbadi, S. H., Sherwin, E. D., Burdeau, P. M., Rutherford, J. S., Chen, Y., Zhang, Z., and Brandt, A. R.: Comparing Continuous Methane Monitoring Technologies for High-Volume Emissions: A Single-Blind Controlled Release Study, ACS EST Air, 1, 871–884, https://doi.org/10.1021/acsestair.4c00015, 2024.

Conrad, B. M., Tyner, D. R., and Johnson, M. R.: Robust probabilities of detection and quantification uncertainty for aerial methane detection: Examples for three airborne technologies, Remote Sensing of Environment, 288, 113499, https://doi.org/10.1016/j.rse.2023.113499, 2023.

El Abbadi, S. H., Chen, Z., Burdeau, P. M., Rutherford, J. S., Chen, Y., Zhang, Z., Sherwin, E. D., and Brandt, A. R.: Technological Maturity of Aircraft-Based Methane Sensing for Greenhouse Gas Mitigation, Environ. Sci. Technol., acs.est.4c02439, https://doi.org/10.1021/acs.est.4c02439, 2024.

FluxLab and Tarek, A.: SIMFLEX-Landfill Methane Controlled-Release Study: Measurement Performance from the Third Experimental Campaign (2025), Environmental Research & Education Foundation, 2026.

Hossain, R. I., Buntov, P., Dudak, Y., Martino, R., Fougère, C., Naseridoust, S., Bourlon, E., Lavoie, M., Khaleghi, A., Hall, C., and Risk, D.: A controlled release experiment for investigating methane measurement performance at landfills, Elem Sci Anth, 14, 00048, https://doi.org/10.1525/elementa.2025.00048, 2026.

Intergovernmental Panel on Climate Change (IPCC) (Ed.): The Earth's Energy Budget, Climate Feedbacks and Climate Sensitivity, in: Climate Change 2021 – The Physical Science Basis: Working Group I Contribution to the Sixth Assessment Report of the Intergovernmental Panel on Climate Change, Cambridge University Press, Cambridge, 923–1054, https://doi.org/10.1017/9781009157896.009, 2023.

Jacob, D. J., Turner, A. J., Maasakkers, J. D., Sheng, J., Sun, K., Liu, X., Chance, K., Aben, I., McKeever, J., and Frankenberg, C.: Satellite observations of atmospheric methane and their value for quantifying methane emissions, Atmos. Chem. Phys., 16, 14371–14396, https://doi.org/10.5194/acp-16-14371-2016, 2016.

Jervis, D., McKeever, J., Durak, B. O. A., Sloan, J. J., Gains, D., Varon, D. J., Ramier, A., Strupler, M., and Tarrant, E.: The GHGSat-D imaging spectrometer, Atmos. Meas. Tech., 14, 2127–2140, https://doi.org/10.5194/amt-14-2127-2021, 2021.

Jervis, D., MacLean, J.-P. W., McKeever, J., Ramier, A., and Strupler, M.: Joint Estimation of the Global Facility-Scale Oil–Gas Methane Emission Rate Distribution and Survey-Mode Detection Probabilities from Multiple Satellite Systems, Environ. Sci. Technol., acs.est.5c17089, https://doi.org/10.1021/acs.est.5c17089, 2026.

Maasakkers, J. D., Varon, D. J., Elfarsdóttir, A., McKeever, J., Jervis, D., Mahapatra, G., Pandey, S., Lorente, A., Borsdorff, T., Foorthuis, L. R., Schuit, B. J., Tol, P., Van Kempen, T. A., Van Hees, R., and Aben, I.: Using satellites to uncover large methane emissions from landfills, Sci. Adv., 8, eabn9683, https://doi.org/10.1126/sciadv.abn9683, 2022.

Manninen, E., Chulakadabba, A., Sargent, M., Zhang, Z., Kamdar, H., Warren, J., Roche, S., Chan Miller, C., Kyzivat, E., Benmergui, J., Pittman, J., Walker, E., Bushey, J., Samra, J., Hawthorne, J., Luo, B., Nasr, M., Sun, K., Franklin, J., Liu, X., Chen, J., and Wofsy, S.: Probabilities of Detection of Methane Plumes by Remote Sensing and Implications for Inferred Emissions Distributions, https://doi.org/10.5194/egusphere-2026-115, 3 February 2026.

McKeever, J. and Jervis, D.: Validation and Metrics for Emissions Detection by Satellite, https://doi.org/10.31223/X5DH9Q, 2 June 2025.

McManemin, A., Juéry, C., Blandin, V., France, J. L., Burdeau, P., and Brandt, A. R.: Controlled release testing of commercially available methane emission measurement technologies at the TADI facility, Atmos. Meas. Tech., 19, 923–934, https://doi.org/10.5194/amt-19-923-2026, 2026.

Ramier, A., Girard, M., Jervis, D., MacLean, J.-P., Marshall, D., Jason McKeever, Mathias Strupler, Ewan Tarrant, and David Young: High-Resolution Methane Detection with the GHGSat Constellation, GLOC 2023, 75002, https://doi.org/10.31223/X5FF0X, 2023.

Rodgers, C. D.: Inverse Methods for Atmospheric Sounding: Theory and Practice, World Scientific, 256 pp., 2000.

Saunois, M., Martinez, A., Poulter, B., Zhang, Z., Raymond, P. A., Regnier, P., Canadell, J. G., Jackson, R. B., Patra, P. K., Bousquet, P., Ciais, P., Dlugokencky, E. J., Lan, X., Allen, G. H., Bastviken, D., Beerling, D. J., Belikov, D. A., Blake, D. R., Castaldi, S., Crippa, M., Deemer, B. R., Dennison, F., Etiope, G., Gedney, N., Höglund-Isaksson, L., Holgerson, M. A., Hopcroft, P. O., Hugelius, G., Ito, A., Jain, A. K., Janardanan, R., Johnson, M. S., Kleinen, T., Krummel, P. B., Lauerwald, R., Li, T., Liu, X., McDonald, K. C., Melton, J. R., Mühle, J., Müller, J., Murguia-Flores, F., Niwa, Y., Noce, S., Pan, S., Parker, R. J., Peng, C., Ramonet, M., Riley, W. J., Rocher-Ros, G., Rosentreter, J. A., Sasakawa, M., Segers, A., Smith, S. J., Stanley, E. H., Thanwerdas, J., Tian, H., Tsuruta, A., Tubiello, F. N., Weber, T. S., Van Der Werf, G. R., Worthy, D. E. J., Xi, Y., Yoshida, Y., Zhang, W., Zheng, B., Zhu, Q., Zhu, Q., and Zhuang, Q.: Global Methane Budget 2000–2020, Earth Syst. Sci. Data, 17, 1873–1958, https://doi.org/10.5194/essd-17-1873-2025, 2025.

Sherwin, E. D., Chen, Y., Ravikumar, A. P., and Brandt, A. R.: Single-blind test of airplane-based hyperspectral methane detection via controlled releases, Elementa: Science of the Anthropocene, 9, 00063, https://doi.org/10.1525/elementa.2021.00063, 2021.

Sherwin, E. D., Rutherford, J. S., Chen, Y., Aminfard, S., Kort, E. A., Jackson, R. B., and Brandt, A. R.: Single-blind validation of space-based point-source detection and quantification of onshore methane emissions, Sci Rep, 13, 3836, https://doi.org/10.1038/s41598-023-30761-2, 2023.

Sherwin, E. D., El Abbadi, S. H., Burdeau, P. M., Zhang, Z., Chen, Z., Rutherford, J. S., Chen, Y., and Brandt, A. R.: Single-blind test of nine methane-sensing satellite systems from three continents, Atmos. Meas. Tech., 17, 765–782, https://doi.org/10.5194/amt-17-765-2024, 2024.

Thorpe, A. K., Frankenberg, C., Aubrey, A. D., Roberts, D. A., Nottrott, A. A., Rahn, T. A., Sauer, J. A., Dubey, M. K., Costigan, K. R., Arata, C., Steffke, A. M., Hills, S., Haselwimmer, C., Charlesworth, D., Funk, C. C., Green, R. O., Lundeen, S. R., Boardman, J. W., Eastwood, M. L., Sarture, C. M., Nolte, S. H., Mccubbin, I. B., Thompson, D. R., and McFadden, J. P.: Mapping methane concentrations from a controlled release experiment using the next generation airborne visible/infrared imaging spectrometer (AVIRIS-NG), Remote Sensing of Environment, 179, 104–115, https://doi.org/10.1016/j.rse.2016.03.032, 2016.

Thorpe, M. J., Kreitinger, A., Altamura, D. T., Dudiak, C. D., Conrad, B. M., Tyner, D. R., Johnson, M. R., Brasseur, J. K., Roos, P. A., Kunkel, W. M., Carre-Burritt, A., Abate, J., Price, T., Yaralian, D., Kennedy, B., Newton, E., Rodriguez, E., Elfar, O. I., and Zimmerle, D. J.: Deployment-invariant probability of detection characterization for aerial LiDAR methane detection, Remote Sensing of Environment, 315, 114435, https://doi.org/10.1016/j.rse.2024.114435, 2024.

Varon, D. J., Jacob, D. J., McKeever, J., Jervis, D., Durak, B. O. A., Xia, Y., and Huang, Y.: Quantifying methane point sources from fine-scale satellite observations of atmospheric methane plumes, Atmos. Meas. Tech., 11, 5673–5686, https://doi.org/10.5194/amt-11-5673-2018, 2018.

Wigle, A., Béliveau, A., Blackmore, D., Lapeyre, P., Osadetz, K., Lemieux, C., and Daun, K. J.: Estimation and Applications of Uncertainty in Methane Emissions Quantification Technologies: A Bayesian Approach, ACS EST Air, 1, 1000–1014, https://doi.org/10.1021/acsestair.4c00030, 2024.